



Robo-SGG: Exploiting Layout-Oriented Normalization and Restitution Can Improve Robust Scene Graph Generation

Changsheng Lv Zijian Fu Mengshi Qi*

State Key Laboratory of Networking and Switching Technology,
Beijing University of Posts and Telecommunications, China

Abstract

In this paper, we propose Robo-SGG, a plug-and-play module for robust scene graph generation (SGG). Unlike standard SGG, the robust scene graph generation aims to perform inference on a diverse range of corrupted images, with the core challenge being the domain shift between the clean and corrupted images. Existing SGG methods suffer from degraded performance due to shifted visual features (e.g., corruption interference or occlusions). To obtain robust visual features, we leverage layout information—representing the global structure of an image—which is robust to domain-shift, to enhance the robustness of SGG methods under corruption. Specifically, we employ Instance Normalization (IN) to alleviate the domain-specific variations and recover the robust structural features (i.e., the positional and semantic relationships among objects) by the proposed Layout-Oriented Restitution. Furthermore, under corrupted images, we introduce a Layout-Embedded Encoder (LEE) that adaptively fuses layout and visual features via a gating mechanism, enhancing the robustness of positional and semantic representations for objects and predicates. Note that our proposed Robo-SGG module is designed as a plug-and-play component, which can be easily integrated into any baseline SGG model. Extensive experiments demonstrate that by integrating the state-of-the-art method into our proposed Robo-SGG, we achieve relative improvements of 6.3%, 11.1%, and 8.0% in mR@50 for PredCls, SGCls, and SGDet tasks on the VG-C benchmark, respectively, and achieve new state-of-the-art performance in the corruption scene graph generation benchmark (VG-C and GQA-C). We will release our source code and model.

“The power of geometry lies in transforming chaotic intuition into clear necessity.”

— Bertrand Russell

1. Introduction

Scene Graph Generation (SGG) [28, 53, 54, 57] has been introduced to create a visually-grounded graph, wherein the nodes represent detected object instances and the edges encapsulate their pairwise relationships. The SGG model has been widely used in many vision tasks, such as autonomous driving [31, 37, 49, 55, 64, 67] and robotic navigation [7, 38, 43, 51].

However, most existing studies in this field assume access to “clean” images, but in real-world scenarios, one encounters various types of impaired data (natural [12], adversarial [18], etc.), with the most prevalent being corruptions that commonly arise from natural phenomena such as noise, blur, various weather conditions, and digital distortions [12], which significantly limits their practical applicability. This highlights the necessity for SGG models to be robust and capable of handling such corruption effectively. In our paper, we focus on the SGG task under image corruptions arising from natural phenomena.

Existing scene graph generation methods [8, 25, 61] leverage visual, textual, and external knowledge graph features to enhance model generalization via multimodal interaction. However, under the interference of corruption, visual features undergo feature domain shifts [15], which erroneously guide the interaction among multimodal information, thereby significantly degrading the performance of SGG models. To improve domain generalization under such shifts, current robust models adopt strategies like data augmentation [13, 62], adversarial training [14, 23, 42], normalization [48, 66], and additional denoising [10] to perform well on both seen and unseen domains with various corruptions. However, these methods introduce considerable computational overhead and are mainly object-centric, failing to enhance the robustness of structural features (i.e., positional and semantic relationships among objects). In contrast, layout information, which captures the global spatial arrangement of objects, is inherently more robust to domain shifts than low-level appearance cues such as texture or color [2]. Consequently, leveraging robust layout rep-

*Corresponding author: qms@bupt.edu.cn.

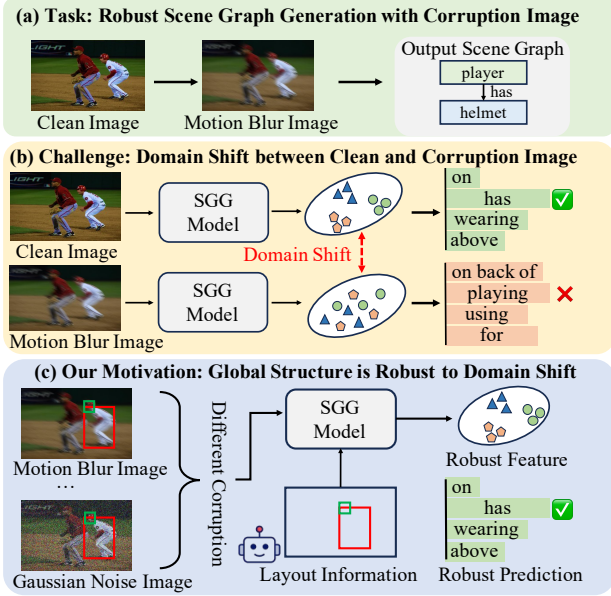


Figure 1. (a) Illustration of the robust SGG task. (b) Feature domain shift between clean and corrupted image features degrades model performance. (c) Robo-SGG leverages layout information to improve the robustness of structural features and object/predicate representations.

representations is particularly well-suited for SGG, which requires comprehensive semantic relationship recognition.

To address this limitation, we propose leveraging the image layout, which captures global structure and is less vulnerable to corruption than low-level features like texture and color, via a newly designed Layout-Oriented Normalization and Restitution Module (NRM) for more robust structural features (see Figure 1 (c)). The key challenge for NRM is to alleviate domain-specific features while retaining robust structural features across different corruptions. We first apply Instance Normalization (IN) to alleviate corruption-specific mean and variance, thereby alleviating domain-specific variations. Subsequently, we propose a layout-aware attention mechanism to capture the image’s structure and recover domain-generalizable structural features based on the attention weights derived from the residual feature, which represents the discrepancy between the original and normalized information.

Furthermore, we propose the Layout-Embedded Encoder (LEE) to obtain robust object and predicate features from individual object bounding boxes and their interactions. Although the existing method SHA [8] explores the fusion of object and predicate spatial and visual information via concatenation, it relies on reliable detection results, which are often inaccurate and noisy under corruptions. In contrast, our proposed LEE learns to downweight unreliable spatial cues and adaptively balances visual and spatial information for robust object and predicate representation under corruption. Specifically, for objects, we use their vi-

sual features to obtain gating coefficients that flexibly fuse the embeddings of bounding box coordinates and visual features. For predicates (*i.e.*, object interactions), we similarly use the visual features extracted from the union region of the object pair as conditions to generate gating coefficients for fusing the embeddings of the object pair’s bounding box coordinates and visual features.

Our main contributions can be summarized as follows:

(1) We propose a novel approach, Robo-SGG, for the robust scene graph generation by designing a Layout-Oriented Normalization and Restitution Module (NRM) to attain a generalized structural feature.

(2) We design a new Layout-Embedded Encoder (LEE), which adaptively fuses the embedding of object bounding box coordinates and visual features via gating to obtain robust object and predicate representations under corruption.

(3) Experimental results demonstrate our proposed Robo-SGG is a plug-and-play method that can be incorporated into any current SGG baselines and show it can achieve relative improvements of 6.3%, 11.1%, and 8.0% in mR@50 for PredCls, SGCls, and SGDet tasks in the VG-C benchmarks, respectively.

2. Related Work

Scene Graph Generation. Scene graphs, originally conceptualized for image retrieval, deconstruct an image into its fundamental elements: objects, their attributes, and the relationships among them [21]. The availability of large-scale datasets like Visual Genome (VG) [24] and GQA [16] has driven significant progress in scene graph generation (SGG) [4, 30, 36, 65]. Recent research addresses challenges such as label bias [39, 40, 44, 46, 50], external knowledge integration [3, 58, 59], semantic relationship modeling [63, 65], and causal reasoning [44, 46], using both one-stage [4, 17] and two-stage [45, 60] framework. The emergence of visual language models (VLMs) has further advanced open-vocabulary SGG [22, 26]. However, most methods assume reliable object detector outputs, which are often unrealistic in the presence of image corruptions. To address this, we enhance object and predicate representations by adaptively balancing detected visual and spatial information, thereby improving SGG robustness in real-world scenarios.

Robustness in Scene Understanding. While most scene understanding models assume clean images, real-world data often contains corruptions that degrade performance. Some works target specific corruptions [10, 29], but general robustness remains challenging. Benchmarks like ImageNet-C [12] evaluate robustness across diverse corruption types. Existing approaches mainly focus on domain adaptation [1, 9, 33] and feature generalization [32, 56, 62], yet often overlook corruption’s impact on inter-object structural features. HiKER [61] recently introduced SGG corruption

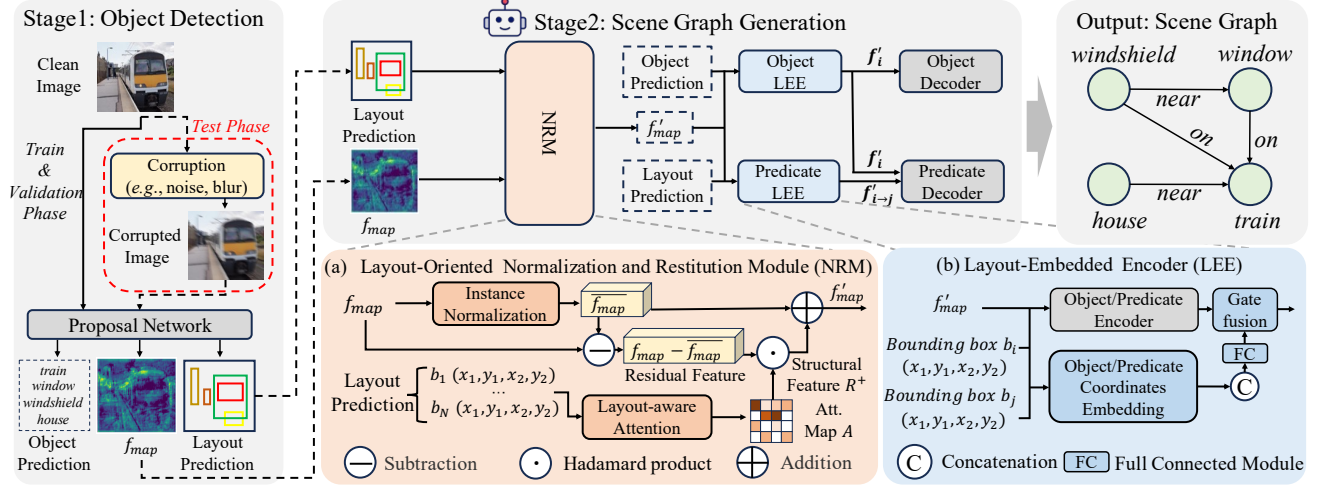


Figure 2. **Overall framework of our proposed Robo-SGG.** Stage 1, Stage 2, and Output denote the standard SGG pipeline, with our NRM and LEE modules integrated into Stage 2. In Stage 1, only clean images are used during training, while corrupted images are employed during validation and testing. Illustrated with a two-stage SGG model: (a) NRM uses Instance Normalization and layout-aware attention to alleviate domain disturbances and restore robust structural features; (b) LEE fuses visual features and bounding box coordinates embedding via gated fusion for robust object and predicate representations.

benchmarks and a knowledge-based robustness method, but its reliance on external knowledge graphs limits flexibility. In contrast, Robo-SGG learns robust, layout-aware structural features that mitigate domain shift caused by corruptions, enabling robust, transferable SGG on corrupted images without extra knowledge graphs.

3. Proposed Method

3.1. Problem Definition

The task of scene graph generation aims to generate a structured representation graph $\mathcal{G} = (\mathcal{O}, \mathcal{E})$ of the given image \mathcal{I} . Each node $o_i \in \mathcal{O}$ in a scene graph represents an object with bounding box $b_i = (x_1, y_1, x_2, y_2)$ and the corresponding category c_i , while each edge $p_{i \rightarrow j} \in \mathcal{E}$ correspond to the predicate category between the object pair (o_i, o_j) . The output of the SGG method is a collection of visual triplets $\langle \text{subject}, \text{predicate}, \text{object} \rangle$, which can be formulated as $\{(o_i, p_{i \rightarrow j}, o_j) \mid o_i, o_j \in \mathcal{O}, p_{i \rightarrow j} \in \mathcal{E}\}$.

3.2. Standard SGG Framework

As shown in Figure 2, our framework is based on the standard SGG pipeline. Notably, our Robo-SGG can be flexibly added to both one-stage [6] and two-stage [60] SGG models, which generally contain three parts: **Proposal Network**, **Object/Predicate Encoder**, and **Object/Predicate Decoder**. The integration of our method into one-stage and two-stage models differs slightly, as discussed in the Proposal Network. Unless otherwise specified, we use the two-stage model as the example in the following description.

Proposal Network. We employ Faster R-CNN [41] with ResNet-101 [11] as the backbone ϕ_f to extract multi-level

feature maps f_{map} from the input image \mathcal{I} . For simplicity, we illustrate our method using a single feature map layer:

$$f_{map} = \phi_f(\mathcal{I}), \quad (1)$$

where $f_{map} \in \mathbb{R}^{C \times H \times W}$, and C, H, W denote the number of channels, height, and width, respectively. In two-stage SGG models, the proposal network outputs $\mathcal{O} = \{o_i\}_{i=1}^N$, where N is the number of detected objects and $o_i = (v_i, b_i, c_i)$ represents the visual feature, bounding box, and category of each object. For one-stage SGG models, our framework utilizes the object proposals and features predicted by the Transformer decoder [6].

Object/Predicate Encoder is used to embed object and predicate features for subsequent modeling and prediction, as follows:

$$f_i = \text{Enc}^{obj}([v_i, \text{Emb}^{lang}(c_i), \text{Emb}^{bbox}(b_i)]) \quad (2)$$

$$f_{i \rightarrow j} = \text{Enc}^{pred}([f_i, v_{i \rightarrow j}, f_j]) \quad (3)$$

where v_i denotes the visual feature of the i -th object, and $v_{i \rightarrow j}$ denotes the visual feature of the union region of objects i and j in the feature map f_{map} . Enc^{obj} and Enc^{pred} denote the object and predicate encoders, which can adopt various encoding modules (e.g., BiLSTM [60]). The operation $[\cdot, \cdot]$ denotes feature concatenation along the feature dimension. $\text{Emb}^{lang}(\cdot)$ embeds the object category c_i into a textual feature vector using a pre-trained language model (e.g., GloVe [35]), while $\text{Emb}^{bbox}(b_i)$ embeds the bounding box b_i into a vector via a fully connected embedding module. Finally, f_i and $f_{i \rightarrow j}$ represent the encoded feature of the i -th object and the encoded predicate feature between objects i and j , respectively.

Object/Predicate Decoder predicts the final object label c'_i and predicate label $p_{i \rightarrow j}$ from the object feature f_i and predicate feature $f_{i \rightarrow j}$, as formulated below:

$$c'_i = \arg \max(\text{Softmax}(\text{Dec}^{obj}(f_i))), \quad (4)$$

$$p_{i \rightarrow j} = \arg \max(\text{Softmax}(\text{Dec}^{pred}(f_{i \rightarrow j}))), \quad (5)$$

where Dec^{obj} and Dec^{pred} denote the object and predicate decoders, respectively, which are typically implemented as a single fully connected module.

3.3. Layout-Oriented Normalization and Restitution Module (NRM)

As depicted in Figure 2(a), we propose the Layout-Oriented Normalization and Restitution Module (NRM), which takes as input the layout information (*i.e.*, all bounding boxes of objects in image \mathcal{I}) and the feature map f_{map} from the backbone ϕ_f , and outputs an enhanced feature map f'_{map} that preserves structural information and is robust to various corruptions. **Our key insight** is that various forms of corruption induce a covariate shift within the feature domain [15], with each type of corruption representing a distinct domain. Consequently, our motivation is to utilize Instance Normalization to alleviate domain-specific disturbances and to enhance the generalization of the structural features in f_{map} across different domains by leveraging the overall structural information, which is less vulnerable to corruption than low-level information like texture and color. The NRM consists of two parts: Instance Normalization and Layout-aware Attention.

Instance Normalization (IN). To address the domain shift in the f_{map} between clean and corrupted images, we employ Instance Normalization (IN) [47] to alleviate the domain-specific disturbance from the feature map f_{map} . Specifically, for each image, we compute the mean and variance for each channel:

$$\mu_i = \frac{1}{HW} \sum_{m=1}^H \sum_{l=1}^W a_{iml}, \sigma_i^2 = \frac{1}{HW} \sum_{m=1}^H \sum_{l=1}^W (a_{iml} - \mu_i)^2, \quad (6)$$

where a_{iml} is the value at channel i and spatial location (m, l) in $f_{map} \in \mathbb{R}^{C \times H \times W}$. Notably, unlike Batch Normalization (BN) [27], which computes statistics across the batch and spatial dimensions, IN computes the mean and variance for each channel of each image over the spatial dimensions only. This approach can effectively alleviate the covariance shift caused by feature domain shift [47]. The instance-normalized feature map $\overline{f_{map}}$ is then computed as:

$$b_{iml} = \frac{a_{iml} - \mu_i}{\sqrt{\sigma_i^2 + \epsilon}}, \quad (7)$$

where a_{iml} and b_{iml} are the values before and after IN, respectively. The residual feature R is computed as:

$$R = f_{map} - \overline{f_{map}}. \quad (8)$$

Layout-aware Attention. While IN alleviate domain-specific disturbances in f_{map} , it may also remove structural features important for SGG. Therefore, we introduce Layout-aware Attention, which utilizes the coordinates of all object bounding boxes to model the global layout and structural patterns within the image. Specifically, let $e_j = (x_j, y_j)$ denote the centroid of the j -th object ($j = 1, 2, \dots, N$). Both the spatial locations (m, l) in the feature map and the object centroids (x_j, y_j) are normalized to the range $[0, 1]$ by dividing by the image width and height, respectively. For each normalized location (m, l) , the attention weight toward object j is defined as:

$$A_{(m,l),j} = \frac{\exp(-\|(m, l) - e_j\|^2)}{\sum_{j'=1}^N \exp(-\|(m, l) - e_{j'}\|^2)}, \quad (9)$$

where $A \in \mathbb{R}^{(H \times W) \times N}$. We then derive a layout mask $M \in \mathbb{R}^{H \times W}$ by taking the maximum attention weight across objects at each location, and the structural feature $R^+ \in \mathbb{R}^{C \times H \times W}$ is denoted:

$$M_{m,l} = \max_j A_{(m,l),j}, R^+ = R \odot M, \quad (10)$$

where \odot denotes broadcasting multiplication across channels. The final output feature map is obtained by combining the instance-normalized feature $\overline{f_{map}}$ and the structural feature R^+ :

$$f'_{map} = \overline{f_{map}} + R^+. \quad (11)$$

This output effectively suppresses domain-specific disturbance while retaining essential structural information.

3.4. Layout-Embedded Encoder (LEE)

As depicted in Figure 2(b), we propose the Object/Predicate Layout-Embedded Encoder (LEE) to enhance the original object and predicate encoders described in Eq. 2 and Eq. 3. LEE consists of two components: Object LEE and Predicate LEE. It establishes a more robust interaction between visual features and bounding box coordinate embeddings, especially under corrupted conditions.

Object/Predicate Coordinate Embedding has been widely adopted in previous works [8], where bounding box coordinates are embedded and concatenated with visual features. Specifically, for an object o_i with bounding box b_i and an object pair (o_i, o_j) , the coordinate embeddings are defined as:

$$f_i^C = \text{Emb}^{obj-bbox}(b_i), \quad (12)$$

$$f_{i \rightarrow j}^C = \text{Emb}^{pred-bbox}([b_i, b_j, e_i - e_j, \|b_i - b_j\|_2]), \quad (13)$$

where $\text{Emb}^{obj-bbox}(\cdot)$ and $\text{Emb}^{pred-bbox}(\cdot)$ are two-layer fully connected embedding modules, e_i is the center of b_i , and $[\cdot, \cdot]$ denotes feature concatenation.

While such coordinate embeddings are effective when the detector provides accurate results, they may introduce noise when the detector outputs unreliable bounding boxes under corrupted images. To address this, we introduce a **Gate Fusion** mechanism that adaptively balances the contributions of visual feature and coordinate embeddings, thereby reducing the impact of inaccurate bounding boxes on SGG performance.

Gate Fusion. We fuse object/predicate features $f_i, f_{i \rightarrow j} \in \mathbb{R}^d$ with their coordinate embeddings $f_i^C, f_{i \rightarrow j}^C \in \mathbb{R}^d$ via gating. For objects, we compute a gate coefficient $z_i \in \mathbb{R}^d$ as:

$$z_i = \text{Sigmoid}(W f_i), \quad (14)$$

where $W \in \mathbb{R}^{d \times d}$ is a learnable parameter, and Sigmoid maps the gate coefficient to $[0, 1]$, indicating the proportion of f_i^C to be retained. The fused feature is then:

$$f'_i = (1 - z_i) \circ f_i^C + z_i \circ f_i, \quad (15)$$

with \circ denoting element-wise multiplication. The same process applies to predicates, yielding $f'_{i \rightarrow j}$. No dimensionality reduction or projection is used, and all features are aligned in the same space d .

3.5. Training and Inference

Loss Function. Following [60], we employ the standard scene graph generation loss function \mathcal{L}_{SGG} , which is the sum of the cross-entropy losses for both predicted objects and predicates. More details are provided in the supplementary materials.

Integration of Robo-SGG into SGG Models. As a plug-and-play method, the NRM component of Robo-SGG can be applied to the f_{map} obtained from Eq. (1), while the Object/Predicate LEE primarily affects the Object/Predicate Encoders in Eq. (2) and Eq. (3). During training, validation, and testing, Robo-SGG can be seamlessly integrated into the corresponding components of existing SGG models.

4. Experiments

4.1. Experimental Settings

Datasets. We use Visual Genome [24] and GQA [16] for both training and testing. To assess robustness, we follow [61] and apply 20 types of corruptions to create VG-C and GQA-C, grouped into five classes [12]: Noise (Gaussian, Shot, Impulse), Blur (Defocus, Glass, Motion, Zoom), Weather1 (Snow, Frost, Fog), Digital (Brightness, Contrast, Elastic, Pixelate, JPEG), and Weather2 (Sunlight Glare, Water Drop, Wildfire Smoke, Rain, Dust). More details and visualizations are in the supplementary materials.

Metrics. For evaluation, we evaluate three popular SGG tasks: 1) Predicate Classification (PredCls), 2) Scene Graph Classification (SGCls), and 3) Scene Graph Detection

(SGDet). To address the pronounced long-tail distribution in the datasets, we adopt the class-balanced mean recall (mR@K) for the top-K predictions per image. We report results for $K = 20, 50$, and 100 .

Compared Methods. To demonstrate the effectiveness of our model-agnostic approach, we integrate Robo-SGG into two categories of SGG models: (1) three baseline two-stage models: MOTIFS [60], VCTree [45], and VTransE [46]; (2) recent state-of-the-art methods: DPL [19] and HiKER-SGG [61], the latter being specifically designed for robust SGG. Additionally, we include the one-stage model RelTR [6] and EGTR [17] for comprehensive evaluation. Notably, following the benchmark protocol in [61], all models (including baselines and ours) are trained on clean images and evaluated on unseen corrupted images.

Implementation Details. All experiments are conducted using PyTorch [34] on V100 GPUs. For MOTIFS [60], VCTree [45], and VTransE [46], we follow the Scene-Graph-Benchmark [46] settings. For DPL [19], HiKER [61], RelTR [6], and EGTR [17], we use the official code. Further details are provided in the supplementary materials.

4.2. Results

Quantitative Results. Table 1 reports results for the three SGG tasks, with models trained on VG and tested on the unseen corruptions in VG-C. After integrating Robo-SGG, all SGG models show less performance degradation in mR@50 and mR@100 across PredCls, SGCls, and SGDet tasks, which demonstrates the robustness of our model in handling corrupted scenarios. For example, with the classic MOTIFS [60], the integration of Robo-SGG reduces the performance drops by 0.6, 0.4, and 0.1 in mR@50 for PredCls, SGCls, and SGDet, respectively. Similar improvements also appear for VCTree [45] and VTransE [46]. Compared to HiKER [61], which is specifically designed for robust SGG under corruptions, our method achieves improvements of 3.7% and 5.7% in mR@50 for PredCls and SGCls, respectively. Furthermore, on the latest state-of-the-art model DPL [19], our method achieves relative gains of 6.3% and 7.5% in mR@50 and mR@100 for the more challenging SGDet task. We also evaluate Robo-SGG on the one-stage model in Figure 4. RelTR [6], where the SGDet mR@50 under corruption improves from 3.4 to 3.7, corresponding to an 8.8% relative gain. While EGTR’s performance in SGDet mR@50 is 17.8/5.6 (clean/corruption), the performance with EGTR+ours improved to 17.8/5.9, achieving a 5.4% relative improvement under VG-C datasets. We further validate the stability of our gains by running MOTIFS+Ours (SGCls) with three random seeds, yielding a standard deviation of less than 0.01, much smaller than the reported improvement (e.g., +11.1% in SGCls).

Qualitative Results. To further demonstrate our method’s effectiveness, Figure 3 shows scene graphs generated by

Method	PredCls			SGCls			SGDet			
	Clean↑	Corruption Avg.↑	Imp.↑	Clean↑	Corruption Avg.↑	Imp.↑	Clean↑	Corruption Avg.↑	Imp.↑	
mR@50	MOTIFS [60]	14.6	12.6	-	11.3	4.5	-	7.2	2.8	-
	MOTIFS+Ours	14.6	13.2	+4.8%	11.4	4.9	+8.8%	7.1	2.9	+3.6%
	VCTree [45]	14.9	12.8	-	12.6	5.4	-	7.3	2.5	-
	VCTree+Ours	15.3	13.6	+6.3%	13.3	6.0	+11.1%	7.3	2.7	+8.3%
	VTransE [46]	14.7	12.1	-	12.6	4.6	-	7.7	2.9	-
	VTransE+Ours	14.9	13.2	+9.0%	12.4	4.9	+6.5%	7.8	3.0	+3.4%
	HiKER [61]	39.3	32.6	-	20.3	3.5	-	-	-	-
	HiKER+Ours	40.8	33.8	+3.7%	21.5	3.7	+5.7%	-	-	-
	DPL [19]	25.5	24.5	-	17.7	7.2	-	12.8	4.8	-
	DPL+Ours	25.7	24.8	+1.1%	19.4	7.8	+8.3%	13.1	5.1	+6.3%
mR@100	MOTIFS [60]	15.8	13.9	-	12.2	4.9	-	8.5	3.4	-
	MOTIFS+Ours	16.1	14.5	+4.3%	12.4	5.1	+3.9%	8.4	3.5	+2.9%
	VCTree [45]	16.1	14.2	-	13.7	5.0	-	8.6	3.1	-
	VCTree+Ours	16.5	15.0	+5.6%	14.4	5.4	+8.0%	8.3	3.3	+6.5%
	VTransE [46]	15.8	13.5	-	13.6	5.9	-	9.2	3.6	-
	VTransE+Ours	16.1	14.4	+6.7%	13.5	6.4	+8.5%	9.2	3.7	+2.8%
	HiKER [61]	41.2	35.1	-	21.4	7.1	-	-	-	-
	HiKER+Ours	42.5	36.4	+3.8%	22.3	7.6	+7.1%	-	-	-
	DPL [19]	28.6	27.6	-	20.2	7.9	-	15.0	5.3	-
	DPL+Ours	28.7	27.9	+1.1%	21.9	8.9	+12.7%	15.4	5.7	+7.5%

Table 1. Comparison of state-of-the-art SGG methods with and without our Robo-SGG module on the clean VG [24] and corrupted VG-C [61] datasets. ‘‘Corruption Avg.’’ denotes the average performance across 20 corruption types at severity level 5. Results with Robo-SGG are highlighted in gray. ‘‘Imp.’’ reports the relative improvement (in **bold**) of ‘‘Corrup. Avg.’’ over the corresponding baseline. The table is divided into two parts: upper for mR@50 and lower for mR@100.

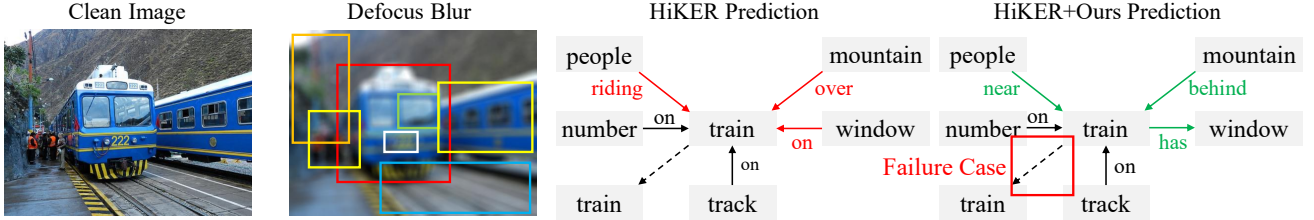


Figure 3. Qualitative comparisons on the PredCls task. Dashed lines: undetected predicates; solid black lines: correct predictions. Red edges: HiKER-SGG errors [61]; green edges: our correct predictions.

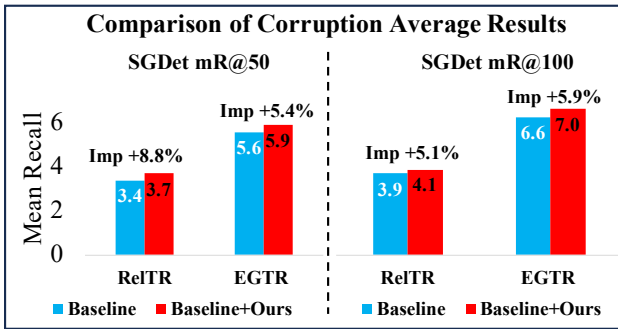


Figure 4. Comparison of state-of-the-art SGG methods with and without our Robo-SGG.

HiKER [61] and HiKER with Robo-SGG on corrupted images. For example, defocus blur visually obscures the boundaries between different objects and reduces the distinction between predicates, causing HiKER to incorrectly predict the triplet as $\langle \text{people-riding-train} \rangle$. In contrast, our method leverages NRM to alleviate the impact of blur on feature maps and utilizes the layout information to recover

the structural features between ‘‘people’’ and ‘‘train’’, resulting in the correct prediction $\langle \text{people-near-train} \rangle$. We also observe a failure case, possibly because both ‘‘near’’ and ‘‘behind’’ can describe the relationship, which could be further addressed with more fine-grained annotations. More examples appear in the supplementary materials.

4.3. Ablation Study

Layout-Oriented Normalization and Restitution Module (NRM). Table 2 compares our NRM with the SNR method [20], which uses channel attention for feature restitution. While SNR improves robustness under corruption (e.g., +2.2% and +2.0% in PredCls mR@100 on MOTIFS [60] and HiKER [61]), our NRM achieves even greater and more consistent gains (+4.3% and +3.8%), demonstrating superior effectiveness in recovering structural features for relationship recognition. Figure 5 further visualizes feature maps under corruption. For example, when contrast corruption causes SNR to focus on irrel-

Task	PredCls						SGCls					
Metric	mR@50			mR@100			mR@50			mR@100		
Method	Clean	Corrup.	Avg. (Imp.)	Clean	Corrup.	Avg. (Imp.)	Clean	Corrup.	Avg. (Imp.)	Clean	Corrup.	Avg. (Imp.)
MOTIFS	14.6	12.6/ -		15.8	13.9/ -		11.3	4.5/-		12.2	4.9/-	
+LEE	14.5	13.0/ (+3.7%)		15.6	14.1/ (+1.4%)		11.3	4.6/ (+2.2%)		12.3	5.0/ (+2.0%)	
+NRM	14.4	12.8/ (+2.0%)		15.5	14.1/ (+1.3%)		11.3	4.7/ (+3.7%)		12.2	5.0/ (+1.9%)	
+LEE + SNR	15.0	12.9/ (+2.4%)		16.2	14.2/ (+2.2%)		11.4	4.6/ (+2.4%)		12.4	5.0/ (+2.1%)	
+LEE + NRM	15.3	13.8/ (+9.5%)		16.0	14.5/ (+4.3%)		11.4	4.9/ (+8.8%)		12.4	5.1/ (+3.9%)	
HiKER [61]	39.3	32.6/-		41.2	35.1/-		20.3	3.5/-		21.4	7.1/-	
+LEE	39.5	32.7/ (+0.3%)		41.5	35.3/ (+0.5%)		20.5	3.5/ (+0.0%)		21.5	7.1/ (+0.0%)	
+NRM	39.5	33.5/ (+2.8%)		41.8	35.9/ (+2.3%)		20.4	3.5/ (+0.6%)		21.5	7.3/ (+2.7%)	
+LEE + SNR	39.4	33.2/ (+1.8%)		41.6	35.8/ (+2.0%)		20.9	3.6/ (+2.9%)		21.8	7.3/ (+2.8%)	
+LEE + NRM	40.8	33.8/ (+3.7%)		42.5	36.4/ (+3.8%)		21.5	3.7/ (+5.7%)		22.3	7.6/ (+7.1%)	

Table 2. Performance comparison of the state-of-the-art SGG methods with integration of our method for the PredCls and SGCls task. “Corrup. Avg.” and “Imp” denote the average performance under different corruption conditions and the performance improvement of our Robo-SGG over the baseline under corruption, respectively, highlighted in **bold**.

Method	GQA-200(mR@20)		
	Clean	Corruption Avg.	Improvement(%)
MOTIFS	20.5	16.0	-
+LEE	21.6	16.3	+1.9%
+LEE + SNR	21.5	17.5	+9.4%
+LEE + NRM	21.7	17.8	+11.3%
VCTree	21.0	16.5	-
+LEE	21.6	17.3	+4.8%
+LEE + SNR	21.5	17.5	+6.1%
+LEE + NRM	21.8	17.9	+8.5%
VTransE	22.5	17.4	-
+LEE	23.0	18.4	+5.7%
+LEE + SNR	22.9	18.6	+6.9%
+LEE + NRM	22.9	19.1	+9.8%

Table 3. Performance comparison of the SGG methods with integration of our method for the PredCls task on GQA [16] dataset.

Method	Clean	Corruption Avg.	Improvement (%)
VCTree	7.32	2.51	-
+LEE _{Add}	7.33	2.48	-1.2
+LEE _{Concat}	7.33	2.46	-2.0
+LEE _{Gate}	7.36	2.62	+4.2
+NRM _{bbox}	7.29	2.55	+1.6
+NRM _{centroid}	7.33	2.69	+7.2

Table 4. Ablation study on different fusion strategies of LEE and different layout-aware attention of NRM (SGDet mR@50).

evant background, NRM suppresses background noise and enhances structural features between objects (e.g., woman-bus, woman-bag), enabling correct predictions such as ⟨woman-hold-bag⟩ and ⟨woman-near-bus⟩. This demonstrates that our Layout-aware Attention more effectively restores structural features essential for scene graph generation. We also ablate the spatial input to the layout-aware attention: using object centroids (NRM_{centroid}) outperforms using full bounding boxes (NRM_{bbox}), as centroids are less sensitive to detection noise.

Setting	Clean	Corruption Avg.	Improvement (%)
30% Bbox Perturbed			
MOTIFS	6.231	2.810	-
+Ours	6.235	2.865	+2.0
Style Change			
MOTIFS	7.051	2.381	-
+Ours	7.064	2.682	+12.6
Distribution Shift (Zero-shot)			
MOTIFS	0.509	0.245	-
+Ours	0.515	0.288	+17.8

Table 5. Robustness under different settings (SGDet mR@50).

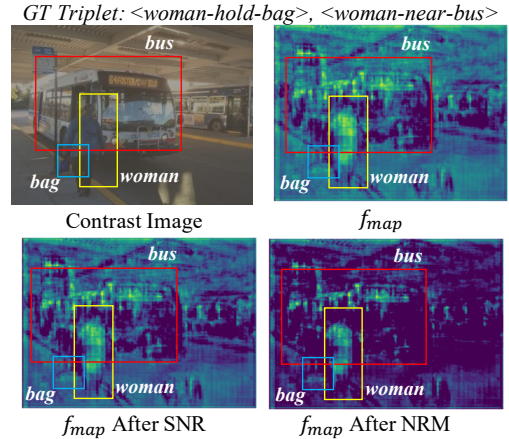


Figure 5. Visualization of corrupted image and its feature maps. The regions of “woman”, “bag”, and “bus” are highlighted with boxes. “GT” denotes Ground Truth.

Layout-Embedded Encoder (LEE). Table 2 shows the impact of Object/Predicate LEE on VG [24] and VG-C [61]. Key findings: 1) On clean VG, adding LEE brings a 0.2% mR@50 gain in both PredCls and SGCls for HiKER [61]. 2) On VG-C, LEE yields larger improvements, with MOTIFS [60] increasing by 3.7% in PredCls and 2.2% in SGCls. Similar results are observed on GQA and GQA-C (Table 3), where both baselines benefit from LEE and NRM. 3)

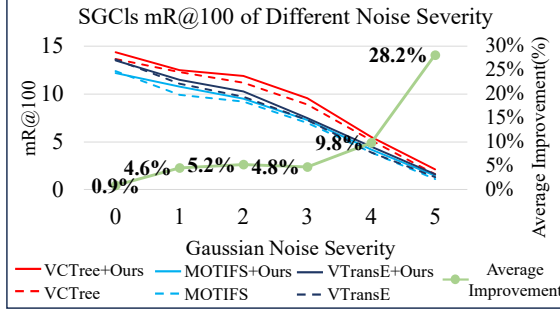


Figure 6. Comparison of baseline and our Robo-SGG under different levels of Gaussian noise.

As Table 4 shows, directly concatenating or adding bounding box embeddings (LEE_{Concat} and LEE_{Add}) under corruption degrades performance due to unreliable detections. In contrast, our gate fusion adaptively downweights noisy box cues and balances visual and spatial information, thus improving robustness in relationship detection and classification. Further analysis reveals that the gating coefficient z_i in Eq. (14) dynamically shifts with corruption severity. Under Gaussian noise, the mean $\mathbb{E}[z_i]$ decreases from 0.65 (severity 1) to 0.52 (severity 5), indicating that LEE increasingly relies on layout cues as visual quality deteriorates. Moreover, when object bounding boxes are perturbed by random noise ($\pm 30\%$ of width and height), our method still improves the baseline by +2.0% (Table 5), demonstrating the effectiveness of the gating mechanism in leveraging global layout structure even under inaccurate detection.

5. How does Robo-SGG help?

Runtime and Memory Overhead. Table 6 shows that LEE and NRM increase inference time by only 0.005s and 0.019s, respectively, on SGCLs. Notably, NRM introduces no extra learnable parameters and does not increase GPU memory usage. LEE adds only 0.02GB of memory during inference. Both modules together achieve an 8.8% mR@50 improvement, which demonstrates a favorable trade-off.

Method	Training		Inference	
	Time/iter	Memory	Time/iter	Memory
MOTIFS	0.777s	13.57GB	0.100s	7.28GB
+LEE	0.800s	16.56GB	0.105s	7.30GB
+NRM	1.036s	13.57GB	0.119s	7.28GB
+LEE+NRM	1.070s	13.56GB	0.127s	7.30GB

Table 6. Cost analysis (per iteration) for SGCLs task.

Analysis of Corruption Severity. We evaluate mR@100 in the SGCLs task under five increasing levels of corruption severity [12] (see Figure 6). As the severity level increases, all methods exhibit performance degradation; however, Robo-SGG consistently outperforms the baseline across all levels. Notably, the relative improvement of our method progressively grows, from 4.6% at severity level 1

Method	SGCLs \uparrow	Imp.(%)	Inference Time \downarrow	Imp.(%)
HiKER	1.5	–	1.75s/image	–
+DDPG [10]	1.7	13.3	43.7s/image	2394.3
+Ours	2.2	46.7	1.79s/image	2.3

Table 7. Comparison between DDPG and our method on motion-blurred images (SGCLs mR@100).

to 28.2% at level 5, demonstrating its increasing effectiveness under more challenging conditions. This trend primarily stems from the NRM’s ability to leverage domain-invariant global layout structures to effectively recover robust structural features even under severe corruption.

Analysis of Other Domain Shift. As shown in Table 5, we further evaluate robustness under other domain shifts. Specifically, we use StyleID [5] to alter image styles, representing another type of domain shift, and also test zero-shot scenarios with mismatched label distributions (Distribution Shift). In both cases, our model achieves strong improvements over MOTIFS, demonstrating its robustness to various distribution changes.

Comparison with Denoising Method. Existing methods such as DDPG [10] address image corruptions like motion blur. We use its pre-trained model to denoise images before SGG, running all experiments on a single Tesla 32 GB V100 GPU. As shown in Table 7, DDPG-denoised images improve performance by 13.3%, but inference time increases by 2394.3%. In contrast, our method achieves a 46.7% gain with only a 2.3% increase in inference time. This is because diffusion-based denoising, while visually appealing, often removes high-frequency details and produces overly smooth images [52], whereas our NRM preserves structural features via Layout-aware Attention for better robustness.

Per-corruption Detailed Results. Our method improves performance across all 20 corruption types, with the largest gains under Noise (Gaussian +31.1%, Shot +28.8%, Impulse +58.7%) and Digital (Pixelate +13.3%, JPEG +63.7%) corruptions. Blur-related degradations (e.g., Defocus +9.6%, Zoom +4.8%) show more limited gains, as blur obscures object boundaries and degrades structural cues. Full results are in the supplementary material.

Error Analysis under Corruption. In SGDet under motion blur, baselines relying solely on distorted visual features may mispredict $\langle \text{man-wearing-shirt} \rangle$ as $\langle \text{man-on-shirt} \rangle$, while those overly dependent on bounding boxes tend to output $\langle \text{man-in-shirt} \rangle$. Our Robo-SGG adaptively fuses both cues, correcting these errors and recovering the correct predicate “wearing”. Full analysis is in the supplementary material.

6. Conclusion

In this paper, we attribute corruption’s impact on scene graph generation to domain shift in image features. We propose Robo-SGG, a plug-and-play module for robust

scene graph generation, consisting of the Layout-Oriented Normalization and Restitution Module for image features and the Layout-Embedded Encoder for object and predicate encoding. Our method easily integrates into existing models and consistently improves multiple baselines. Extensive experiments on VG-C and GQA-C benchmarks demonstrate its effectiveness and state-of-the-art performance.

References

- [1] Philipp Benz, Chaoning Zhang, Adil Karjauv, and In So Kweon. Revisiting batch normalization for improving corruption robustness. In *Proceedings of the IEEE/CVF winter conference on applications of computer vision*, pages 494–503, 2021. 2
- [2] Galal M Binmakhshen and Sabri A Mahmoud. Document layout analysis: a comprehensive survey. *ACM Computing Surveys (CSUR)*, 52(6):1–36, 2019. 1
- [3] Zhanwen Chen, Saed Rezayi, and Sheng Li. More knowledge, less bias: Unbiasing scene graph generation with explicit ontological adjustment. In *Proceedings of the IEEE/CVF Winter Conference on Applications of Computer Vision*, pages 4023–4032, 2023. 2
- [4] Zuyao Chen, Jinlin Wu, Zhen Lei, Zhaoxiang Zhang, and Chang Wen Chen. Expanding scene graph boundaries: fully open-vocabulary scene graph generation via visual-concept alignment and retention. In *European Conference on Computer Vision*, pages 108–124. Springer, 2024. 2
- [5] Jiwoo Chung, Sangeek Hyun, and Jae-Pil Heo. Style injection in diffusion: A training-free approach for adapting large-scale diffusion models for style transfer. In *Proceedings of the IEEE/CVF conference on computer vision and pattern recognition*, pages 8795–8805, 2024. 8
- [6] Yuren Cong, Michael Ying Yang, Bodo Rosenhahn, and Bodo Rosenhahn. Reltr: Relation transformer for scene graph generation. *IEEE Transactions on Pattern Analysis and Machine Intelligence*, 45(9):11169–11183, 2023. 3, 5
- [7] Wei Deng, Mengshi Qi, and Huadong Ma. Global-local tree search in vlms for 3d indoor scene generation. In *Proceedings of the Computer Vision and Pattern Recognition Conference*, pages 8975–8984, 2025. 1
- [8] Xingning Dong, Tian Gan, Xuemeng Song, Jianlong Wu, Yuan Cheng, and Liqiang Nie. Stacked hybrid-attention and group collaborative learning for unbiased scene graph generation. In *Proceedings of the IEEE/CVF Conference on Computer Vision and Pattern Recognition*, pages 19427–19436, 2022. 1, 2, 4
- [9] Jin Gao, Jialing Zhang, Xihui Liu, Trevor Darrell, Evan Shelhamer, and Dequan Wang. Back to the source: Diffusion-driven adaptation to test-time corruption. In *Proceedings of the IEEE/CVF Conference on Computer Vision and Pattern Recognition*, pages 11786–11796, 2023. 2
- [10] Tomer Garber and Tom Tirer. Image restoration by denoising diffusion models with iteratively preconditioned guidance. In *Proceedings of the IEEE/CVF Conference on Computer Vision and Pattern Recognition*, pages 25245–25254, 2024. 1, 2, 8
- [11] Kaiming He, Xiangyu Zhang, Shaoqing Ren, and Jian Sun. Deep residual learning for image recognition. In *Proceedings of the IEEE conference on computer vision and pattern recognition*, pages 770–778, 2016. 3
- [12] Dan Hendrycks, Thomas Dietterich, Thomas Dietterich, and Thomas Dietterich. Benchmarking neural network robustness to common corruptions and perturbations. *arXiv preprint arXiv:1903.12261*, 2019. 1, 2, 5, 8
- [13] Dan Hendrycks, Norman Mu, Ekin D Cubuk, Barret Zoph, Justin Gilmer, and Balaji Lakshminarayanan. Augmix: A simple data processing method to improve robustness and uncertainty. *arXiv preprint arXiv:1912.02781*, 2019. 1
- [14] Charles Herrmann, Kyle Sargent, Lu Jiang, Ramin Zabih, Huiwen Chang, Ce Liu, Dilip Krishnan, and Deqing Sun. Pyramid adversarial training improves vit performance. In *Proceedings of the IEEE/CVF conference on computer vision and pattern recognition*, pages 13419–13429, 2022. 1
- [15] Lei Huang, Jie Qin, Yi Zhou, Fan Zhu, Li Liu, and Ling Shao. Normalization techniques in training dnns: Methodology, analysis and application. *IEEE transactions on pattern analysis and machine intelligence*, 45(8):10173–10196, 2023. 1, 4
- [16] Drew A Hudson and Christopher D Manning. Gqa: A new dataset for real-world visual reasoning and compositional question answering. In *Proceedings of the IEEE/CVF conference on computer vision and pattern recognition*, pages 6700–6709, 2019. 2, 5, 7
- [17] Jinbae Im, JeongYeon Nam, Nokyoung Park, Hyungmin Lee, and Seunghyun Park. Egtr: Extracting graph from transformer for scene graph generation. In *Proceedings of the IEEE/CVF Conference on Computer Vision and Pattern Recognition*, pages 24229–24238, 2024. 2, 5
- [18] Shinji Ito. On optimal robustness to adversarial corruption in online decision problems. *Advances in Neural Information Processing Systems*, 34:7409–7420, 2021. 1
- [19] Jaehyeong Jeon, Kibum Kim, Kanghoon Yoon, and Chanyoung Park. Semantic diversity-aware prototype-based learning for unbiased scene graph generation. In *European Conference on Computer Vision*, pages 379–395. Springer, 2024. 5, 6
- [20] Xin Jin, Cuiling Lan, Wenjun Zeng, Zhibo Chen, and Li Zhang. Style normalization and restitution for generalizable person re-identification. In *Proceedings of the IEEE/CVF conference on computer vision and pattern recognition*, pages 3143–3152, 2020. 6
- [21] Justin Johnson, Ranjay Krishna, Michael Stark, Li-Jia Li, David Shamma, Michael Bernstein, and Li Fei-Fei. Image retrieval using scene graphs. In *Proceedings of the IEEE conference on computer vision and pattern recognition*, pages 3668–3678, 2015. 2
- [22] Kibum Kim, Kanghoon Yoon, Jaehyeong Jeon, Yeonjun In, Jinyoung Moon, Donghyun Kim, and Chanyoung Park. Llm4sgg: large language models for weakly supervised scene graph generation. In *Proceedings of the IEEE/CVF Conference on Computer Vision and Pattern Recognition*, pages 28306–28316, 2024. 2
- [23] Klim Kireev, Maksym Andriushchenko, and Nicolas Flammarion. On the effectiveness of adversarial training against

- common corruptions. In *Uncertainty in Artificial Intelligence*, pages 1012–1021. PMLR, 2022. 1
- [24] Ranjay Krishna, Yuke Zhu, Oliver Groth, Justin Johnson, Kenji Hata, Joshua Kravitz, Stephanie Chen, Yannis Kalantidis, Li-Jia Li, David A Shamma, et al. Visual genome: Connecting language and vision using crowdsourced dense image annotations. *International journal of computer vision*, 123(1):32–73, 2017. 2, 5, 6, 7
- [25] Jiankai Li, Yunhong Wang, Xiefan Guo, Ruijie Yang, and Weixin Li. Leveraging predicate and triplet learning for scene graph generation. In *Proceedings of the IEEE/CVF Conference on Computer Vision and Pattern Recognition*, pages 28369–28379, 2024. 1
- [26] Rongjie Li, Songyang Zhang, Dahua Lin, Kai Chen, and Xuming He. From pixels to graphs: Open-vocabulary scene graph generation with vision-language models. In *Proceedings of the IEEE/CVF Conference on Computer Vision and Pattern Recognition*, pages 28076–28086, 2024. 2
- [27] Yanghao Li, Naiyan Wang, Jianping Shi, Jiaying Liu, and Xiaodi Hou. Revisiting batch normalization for practical domain adaptation. *arXiv preprint arXiv:1603.04779*, 2016. 4
- [28] Yikang Li, Wanli Ouyang, Bolei Zhou, Kun Wang, and Xiaogang Wang. Scene graph generation from objects, phrases and region captions. In *Proceedings of the IEEE international conference on computer vision*, pages 1261–1270, 2017. 1
- [29] Jingbo Lin, Zhilu Zhang, Yuxiang Wei, Dongwei Ren, Dongsheng Jiang, Qi Tian, and Wangmeng Zuo. Improving image restoration through removing degradations in textual representations. In *Proceedings of the IEEE/CVF Conference on Computer Vision and Pattern Recognition*, pages 2866–2878, 2024. 2
- [30] Hengyue Liu, Ning Yan, Masood Mortazavi, and Bir Bhanu. Fully convolutional scene graph generation. In *Proceedings of the IEEE/CVF Conference on Computer Vision and Pattern Recognition*, pages 11546–11556, 2021. 2
- [31] Changsheng Lv, Mengshi Qi, Liang Liu, and Huadong Ma. T2sg: Traffic topology scene graph for topology reasoning in autonomous driving. In *Proceedings of the Computer Vision and Pattern Recognition Conference*, pages 17197–17206, 2025. 1
- [32] Eric Mintun, Alexander Kirillov, and Saining Xie. On interaction between augmentations and corruptions in natural corruption robustness. *Advances in Neural Information Processing Systems*, 34:3571–3583, 2021. 2
- [33] M Jehanzeb Mirza, Jakub Micorek, Horst Possegger, and Horst Bischof. The norm must go on: Dynamic unsupervised domain adaptation by normalization. In *Proceedings of the IEEE/CVF conference on computer vision and pattern recognition*, pages 14765–14775, 2022. 2
- [34] Adam Paszke, Sam Gross, Francisco Massa, Adam Lerer, James Bradbury, Gregory Chanan, Trevor Killeen, Zeming Lin, Natalia Gimelshein, Luca Antiga, et al. Pytorch: An imperative style, high-performance deep learning library. *Advances in Neural Information Processing Systems*, 32, 2019. 5
- [35] Jeffrey Pennington, Richard Socher, Christopher D Manning, and Christopher D. Glove: Global vectors for word representation. In *Proceedings of the 2014 conference on empirical methods in natural language processing (EMNLP)*, pages 1532–1543, 2014. 3
- [36] Mengshi Qi, Weijian Li, Zhengyuan Yang, Yunhong Wang, and Jiebo Luo. Attentive relational networks for mapping images to scene graphs. In *Proceedings of the IEEE/CVF Conference on Computer Vision and Pattern Recognition*, pages 3957–3966, 2019. 2
- [37] Mengshi Qi, Yunhong Wang, Annan Li, and Jiebo Luo. Stcgan: Spatio-temporally coupled generative adversarial networks for predictive scene parsing. *IEEE Transactions on Image Processing*, 29:5420–5430, 2020. 1
- [38] Mengshi Qi, Jie Qin, Yi Yang, Yunhong Wang, and Jiebo Luo. Semantics-aware spatial-temporal binaries for cross-modal video retrieval. *IEEE Transactions on Image Processing*, 30:2989–3004, 2021. 1
- [39] Mengshi Qi, Changsheng Lv, and Huadong Ma. Robust disentangled counterfactual learning for physical audiovisual commonsense reasoning. *IEEE Transactions on Pattern Analysis and Machine Intelligence*, pages 1–14, 2025. 2
- [40] Mengshi Qi, Hao Ye, Jiaxuan Peng, and Huadong Ma. Action quality assessment via hierarchical pose-guided multi-stage contrastive regression. *IEEE Transactions on Image Processing*, 34:6461–6474, 2025. 2
- [41] Shaoqing Ren, Kaiming He, Ross Girshick, and Jian Sun. Faster r-cnn: Towards real-time object detection with region proposal networks. *IEEE transactions on pattern analysis and machine intelligence*, 39(6):1137–1149, 2016. 3
- [42] Evgenia Rusak, Lukas Schott, Roland S Zimmermann, Julian Bitterwolf, Oliver Bringmann, Matthias Bethge, and Wieland Brendel. A simple way to make neural networks robust against diverse image corruptions. In *Computer Vision—ECCV 2020: 16th European Conference, Glasgow, UK, August 23–28, 2020, Proceedings, Part III 16*, pages 53–69. Springer, 2020. 1
- [43] Kunal Pratap Singh, Jordi Salvador, Luca Weihs, and Aniruddha Kembhavi. Scene graph contrastive learning for embodied navigation. In *Proceedings of the IEEE/CVF International Conference on Computer Vision*, pages 10884–10894, 2023. 1
- [44] Shuzhou Sun, Shuaifeng Zhi, Qing Liao, Janne Heikkilä, and Li Liu. Unbiased scene graph generation via two-stage causal modeling. *IEEE Transactions on Pattern Analysis and Machine Intelligence*, 45(10):12562–12580, 2023. 2
- [45] Kaihua Tang, Hanwang Zhang, Baoyuan Wu, Wenhan Luo, and Wei Liu. Learning to compose dynamic tree structures for visual contexts. In *Proceedings of the IEEE/CVF conference on computer vision and pattern recognition*, pages 6619–6628, 2019. 2, 5, 6
- [46] Kaihua Tang, Yulei Niu, Jianqiang Huang, Jiaxin Shi, and Hanwang Zhang. Unbiased scene graph generation from biased training. In *Proceedings of the IEEE/CVF conference on computer vision and pattern recognition*, pages 3716–3725, 2020. 2, 5, 6
- [47] D Ulyanov. Instance normalization: The missing ingredient for fast stylization. *arXiv preprint arXiv:1607.08022*, 2016. 4

- [48] Dequan Wang, Evan Shelhamer, Shaoteng Liu, Bruno Olshausen, and Trevor Darrell. Tent: Fully test-time adaptation by entropy minimization. *arXiv preprint arXiv:2006.10726*, 2020. 1
- [49] Junyao Wang, Arnav Vaibhav Malawade, Junhong Zhou, Shih-Yuan Yu, and Mohammad Abdullah Al Faruque. Rs2g: Data-driven scene-graph extraction and embedding for robust autonomous perception and scenario understanding. In *Proceedings of the IEEE/CVF Winter Conference on Applications of Computer Vision*, pages 7493–7502, 2024. 1
- [50] Rui Wang, Mengshi Qi, Yingxia Shao, Anfu Zhou, and Huadong Ma. Pitn: Physics-informed temporal networks for cuffless blood pressure estimation. *IEEE Transactions on Mobile Computing*, pages 1–14, 2025. 2
- [51] Abdelrhman Werby, Chenguang Huang, Martin Büchner, Abhinav Valada, and Wolfram Burgard. Hierarchical open-vocabulary 3d scene graphs for language-grounded robot navigation. In *First Workshop on Vision-Language Models for Navigation and Manipulation at ICRA 2024*, 2024. 1
- [52] Jay Whang, Mauricio Delbracio, Hossein Talebi, Chitwan Saharia, Alexandros G Dimakis, and Peyman Milanfar. Deblurring via stochastic refinement. In *Proceedings of the IEEE/CVF conference on computer vision and pattern recognition*, pages 16293–16303, 2022. 8
- [53] Danfei Xu, Yuke Zhu, Christopher B Choy, and Li Fei-Fei. Scene graph generation by iterative message passing. In *Proceedings of the IEEE conference on computer vision and pattern recognition*, pages 5410–5419, 2017. 1
- [54] Jianwei Yang, Jiasen Lu, Stefan Lee, Dhruv Batra, and Devi Parikh. Graph r-cnn for scene graph generation. In *Proceedings of the European conference on computer vision (ECCV)*, pages 670–685, 2018. 1
- [55] Hao Ye, Mengshi Qi, Zhaohong Liu, Liang Liu, and Huadong Ma. Safedriverag: Towards safe autonomous driving with knowledge graph-based retrieval-augmented generation. In *Proceedings of the 33rd ACM International Conference on Multimedia*, pages 11170–11178, 2025. 1
- [56] Dong Yin, Raphael Gontijo Lopes, Jon Shlens, Ekin Dogus Cubuk, and Justin Gilmer. A fourier perspective on model robustness in computer vision. *Advances in Neural Information Processing Systems*, 32, 2019. 2
- [57] Ruichi Yu, Ang Li, Vlad I Morariu, and Larry S Davis. Visual relationship detection with internal and external linguistic knowledge distillation. In *Proceedings of the IEEE/CVF International Conference on Computer Vision*, pages 1974–1982, 2017. 1
- [58] Alireza Zareian, Svebor Karaman, and Shih-Fu Chang. Bridging knowledge graphs to generate scene graphs. In *Computer Vision—ECCV 2020: 16th European Conference, Glasgow, UK, August 23–28, 2020, Proceedings, Part XXIII 16*, pages 606–623. Springer, 2020. 2
- [59] Alireza Zareian, Zhecan Wang, Haoxuan You, and Shih-Fu Chang. Learning visual commonsense for robust scene graph generation. In *European Conference on Computer Vision*, pages 642–657. Springer, 2020. 2
- [60] Rowan Zellers, Mark Yatskar, Sam Thomson, and Yejin Choi. Neural motifs: Scene graph parsing with global context. In *Proceedings of the IEEE conference on computer vision and pattern recognition*, pages 5831–5840, 2018. 2, 3, 5, 6, 7
- [61] Ce Zhang, Simon Stepputtis, Joseph Campbell, Katia Sycara, and Yaqi Xie. Hiker-sgg: Hierarchical knowledge enhanced robust scene graph generation. In *Proceedings of the IEEE/CVF Conference on Computer Vision and Pattern Recognition*, pages 28233–28243, 2024. 1, 2, 5, 6, 7
- [62] Marvin Zhang, Sergey Levine, and Chelsea Finn. Memo: Test time robustness via adaptation and augmentation. *Advances in neural information processing systems*, 35:38629–38642, 2022. 1, 2
- [63] Yong Zhang, Yingwei Pan, Ting Yao, Rui Huang, Tao Mei, and Chang-Wen Chen. Learning to generate language-supervised and open-vocabulary scene graph using pre-trained visual-semantic space. In *Proceedings of the IEEE/CVF Conference on Computer Vision and Pattern Recognition*, pages 2915–2924, 2023. 2
- [64] Yunpeng Zhang, Deheng Qian, Ding Li, Yifeng Pan, Yong Chen, Zhenbao Liang, Zhiyao Zhang, Shurui Zhang, Hongxu Li, Maolei Fu, et al. Graphad: Interaction scene graph for end-to-end autonomous driving. *arXiv preprint arXiv:2403.19098*, 2024. 1
- [65] Chaofan Zheng, Xinyu Lyu, Lianli Gao, Bo Dai, and Jingkuan Song. Prototype-based embedding network for scene graph generation. In *Proceedings of the IEEE/CVF Conference on Computer Vision and Pattern Recognition*, pages 22783–22792, 2023. 2
- [66] Kaiyang Zhou, Yongxin Yang, Andrea Cavallaro, and Tao Xiang. Omni-scale feature learning for person re-identification. In *Proceedings of the IEEE/CVF international conference on computer vision*, pages 3702–3712, 2019. 1
- [67] Pengfei Zhu, Mengshi Qi, Xia Li, Weijian Li, and Huadong Ma. Unsupervised self-driving attention prediction via uncertainty mining and knowledge embedding. In *Proceedings of the IEEE/CVF International Conference on Computer Vision*, pages 8558–8568, 2023. 1